The Innovation Geoscience

Supplementary Materials for

Cenozoic destruction of eastern North China craton evidenced by seismically imaged lithosphere delamination and geochemistry data

This PDF file includes:

Methods and materials
Figs. S1 to S15
References

Methods and materials

1. Joint inversion of body wave arrival times, surface wave dispersion data and receiver functions

In this study, we adopted the joint inversion method of Han et al. (2022a) to jointly use body wave arrival times, surface wave dispersion data and receiver functions to simultaneously invert Vp, Vs models and relocate seismic events. The joint inversion system is based on the double-difference seismic tomography system (Zhang and Thurber, 2003, 2006), joint inversion system of body wave arrival times and surface wave dispersion data (Zhang et al., 2014; Fang et al., 2016; Han et al., 2022b), and joint inversion system of surface wave dispersion data and receiver functions (Julia et al., 2000). The joint inversion system of Han et al. (2022a) is represented as follows:

$$\begin{bmatrix} \mathbf{G}_{\mathrm{H}}^{\mathrm{T_p}} & \mathbf{G}_{\mathrm{V_p}}^{\mathrm{T_p}} & 0 \\ \mathbf{G}_{\mathrm{H}}^{\mathrm{T_s}} & 0 & \mathbf{G}_{\mathrm{V_s}}^{\mathrm{T_s}} \\ 0 & \alpha\mathbf{G}_{\mathrm{V_p}}^{\mathrm{sw}} & \alpha\mathbf{G}_{\mathrm{V_s}}^{\mathrm{sw}} \\ 0 & 0 & \beta\mathbf{G}_{\mathrm{V_s}}^{\mathrm{RF}} \\ 0 & \eta_1\mathbf{L} & 0 \\ 0 & 0 & \eta_2\mathbf{L} \end{bmatrix} \begin{bmatrix} \Delta\mathbf{H} \\ \Delta\mathbf{m}_{\mathrm{p}} \\ \Delta\mathbf{m}_{\mathrm{s}} \end{bmatrix} = \begin{bmatrix} \mathbf{d}^{\mathrm{T_p}} \\ \mathbf{d}^{\mathrm{T_s}} \\ \boldsymbol{\alpha}\mathrm{d}^{\mathrm{sw}} \\ \beta\mathbf{d}^{\mathrm{RF}} \\ 0 \\ 0 \end{bmatrix} \tag{1}$$

where $\Delta\mathrm{H}$, $\Delta\mathrm{m_p}$, and $\Delta\mathrm{m_s}$ are the perturbations for source parameters (origin time and location), Vp and Vs. The first two rows represent inversion system for body wave arrival times, with $\mathrm{d}^{\mathrm{T_p}}$ and $\mathrm{d}^{\mathrm{T_s}}$ being P- and S-wave arrival time residual vectors, $\mathrm{G}_{\mathrm{H}}^{\mathrm{T_p}}$ (or $\mathrm{G}_{\mathrm{H}}^{\mathrm{T_s}}$) representing the partial derivative matrix of P (or S) arrival times with respect to source parameters, and $\mathrm{G}_{\mathrm{V_p}}^{\mathrm{T_p}}$ (or $\mathrm{G}_{\mathrm{V_s}}^{\mathrm{T_s}}$) partial derivative matrix of P (or S) arrival times relative to the Vp (or Vs) model. The third row indicates the inversion system for surface wave data, in which d^{sw} is the residual vector of the surface wave dispersion data, $\mathrm{G}_{\mathrm{V_p}}^{\mathrm{sw}}$and $\mathrm{G}_{\mathrm{V_s}}^{\mathrm{sw}}$ are the partial derivative matrices of surface wave data relative to the Vp and Vs models, respectively. The fourth row denotes the receiver function inversion system, in which the $\mathbf{d}^{\mathrm{RF}}$ is the residual vector of the receiver function data, $\mathbf{G}_{\mathrm{V_s}}^{\mathrm{RF}}$ is the partial derivative matrix of the receiver function data relative to the Vs model. Parameters α and β are the weights of surface wave data and receiver functions in the joint inversion system. The last two rows represent regularizations, where **L** is the first-order Tikhonov smoothing matrix, and η_1 and η_2 are the smoothing weights for Vp and Vs models, respectively. This joint inversion system can be solved by the LSQR algorithm (Paige and Saunders, 1982), where damping regularization is used.

The joint inversion system of Han et al. (2022a) has considered the following factors to improve the reliability of Vp and Vs models, mainly including: (1) topographic variations are considered when calculating surface wave and receiver function sensitive matrices, and (2) sensitivity of surface wave dispersion data to Vp structure is also considered. Synthetic tests have shown that this joint inversion system can better constrain the Vs model and improve its depth resolution by incorporating receiver functions (Han et al., 2022a; Zhang et al., 2023).

2. Determining lithosphere velocity model of North China Craton by joint seismic inversion

For body wave arrival times, we collected first arrivals for a total of 30,296 earthquakes recorded by 493 stations for the period of October 2008 to June 2018. The distribution of events and stations is shown in Fig. 1. After a strict quality control process, 321,416 P-wave and 298,523 S-wave first arrival times are obtained. The travel time curves for P- and S-waves are shown in Fig. S1. Based on absolute arrival times, 770,652 P-wave and 718,783 S-wave differential travel times from event pairs are constructed. The surface wave dispersion data come from Shen et al. (2016), which mainly consists of Rayleigh wave group and phase velocities at periods of 8-50s, which have the lateral resolutions of 0.5°×0.5° (Fig. S2-S3). This set of surface wave data has a good coverage in the North China region and can provide good constraints on the lithospheric structure of the NCC.

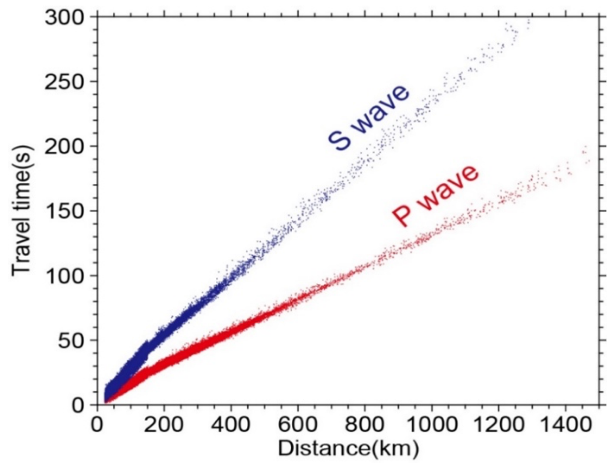

Figure S1. Travel time curves of P (red) and S (blue) waves for the arrival time dataset in the NCC.

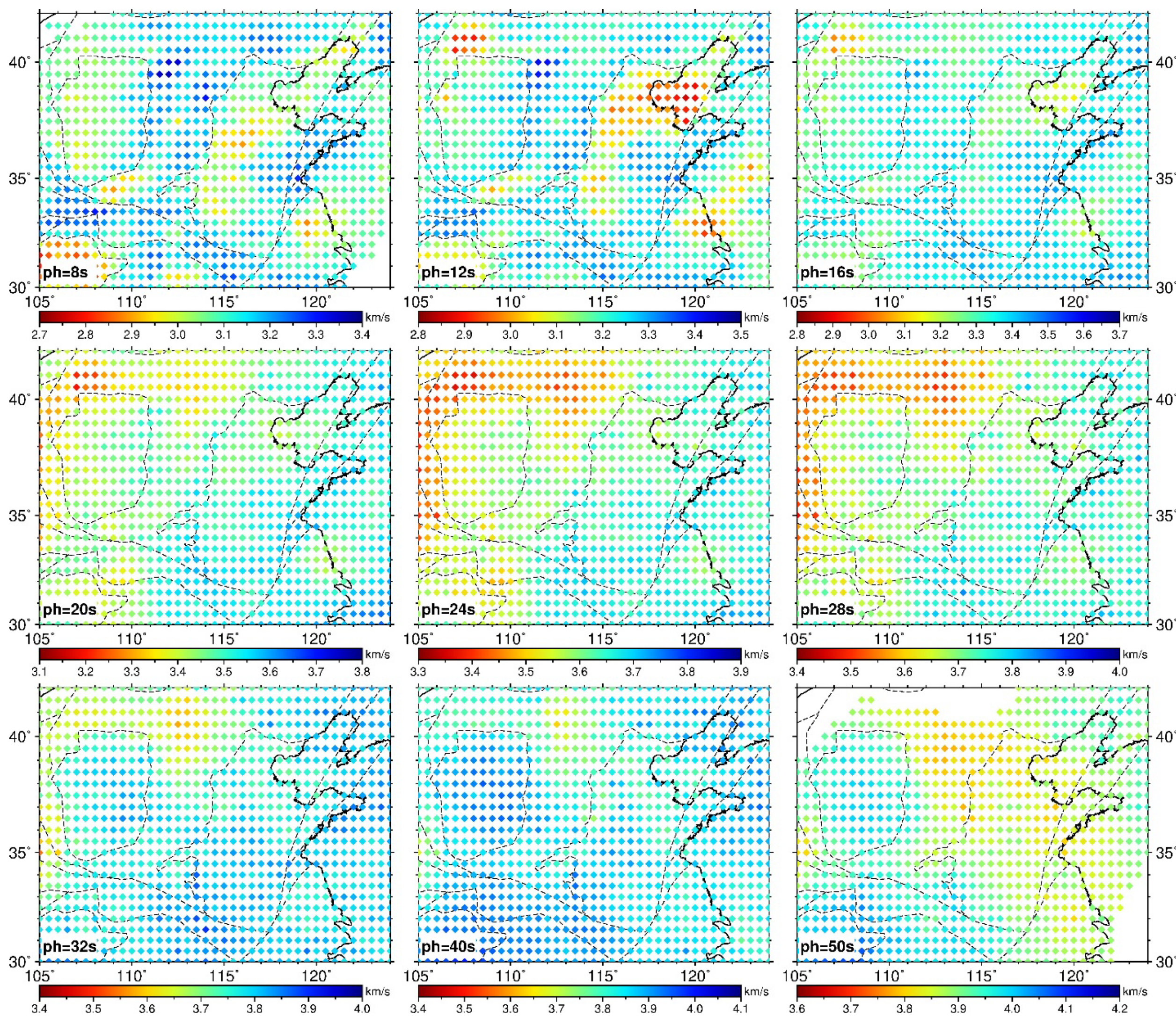

Figure S2. The distribution of surface wave phase velocity maps at periods from 8s to 50s

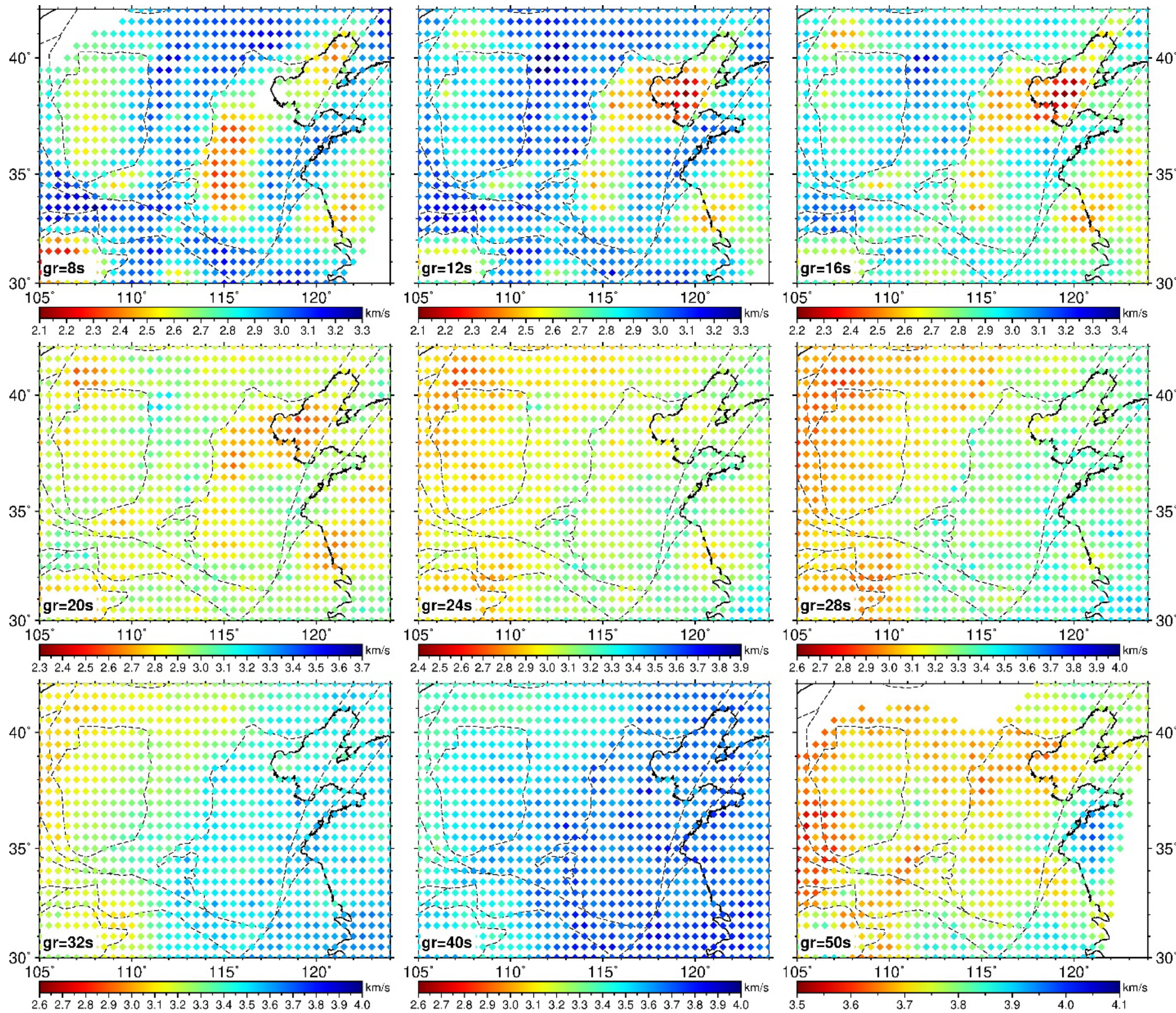

Figure S3. The distribution of surface wave group velocity distribution from 8s to 50s

For the receiver functions, we selected teleseismic three-component waveforms for earthquakes with magnitudes greater than 5.5 and epicentral distances between 30° and 90°. The time domain iterative deconvolution method (Ligorrfa and Ammon, 1999) is used to extract the receiver functions. The Gaussian filter factor is selected as 1.0, with the sampling interval of 0.1s. We further interpolated receiver functions by the inverse distance weighted interpolation method (Chai et al., 2015) to obtain smooth receiver functions. Fig. S4 shows interpolated receiver functions at time slices at 1s, 3s, 5s and 7s. It can be seen that the interpolated receiver functions have a good lateral continuity.

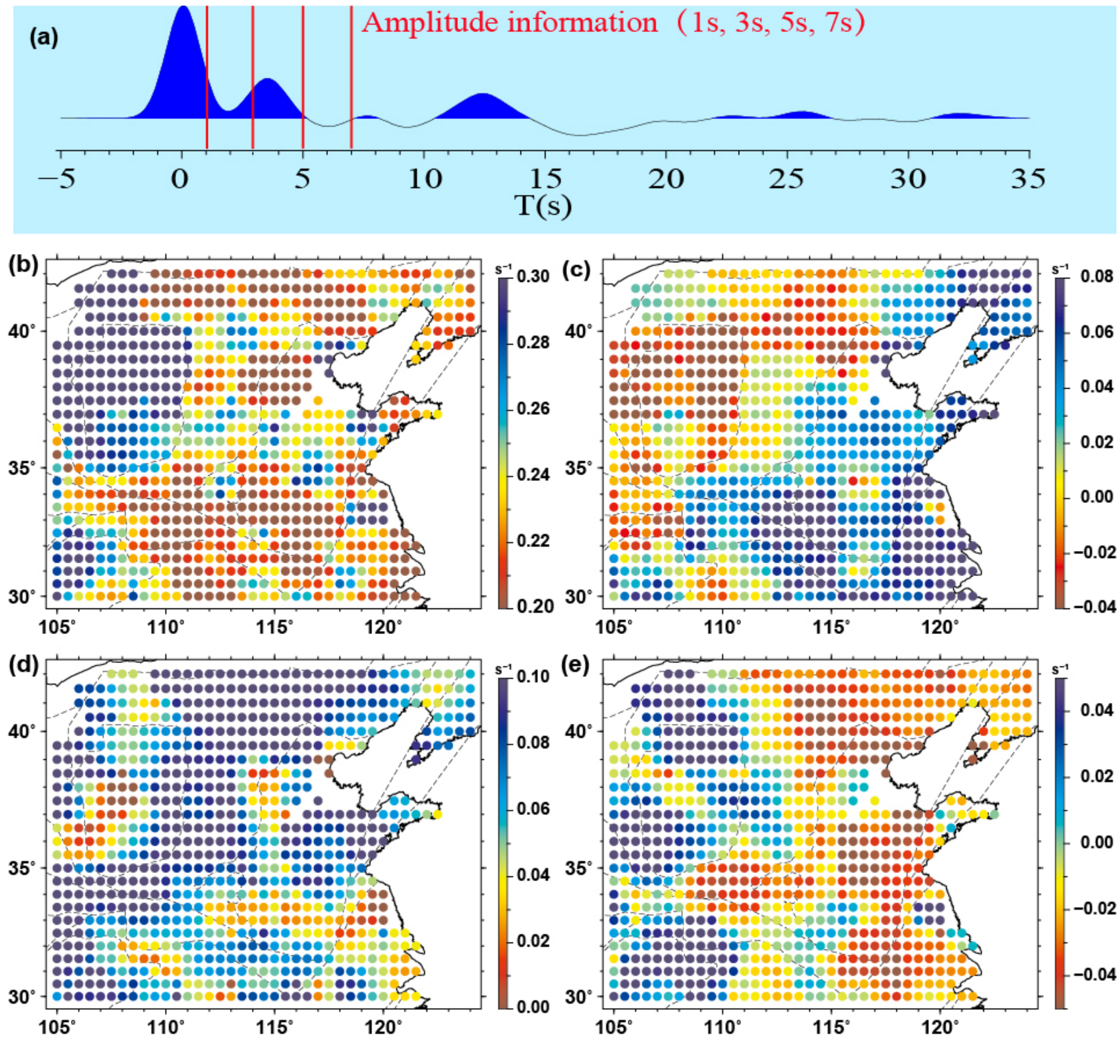

Figure S4. Interpolated receiver functions at 1s,3s,5s and 7s for north China. (a) One example of teleseismic receiver function from -5s to 35s at a seismic station in north China. Timing at 1 s, 3 s, 5 s and 7 s is marked by red lines. (b), (c), (d) and (e) show the distribution of amplitudes of interpolated receiver functions at 1s,3s,5s and 7s, respectively.

We use the USTClitho1.0 Vp and Vs models (Xin et al., 2019) as the initial models for joint seismic inversion. The grid intervals in longitude and latitude are 0.5°, and in the depth direction vary from 5 km in the depth range of 0 to 80 km and 15 km in the depth range of 80 to 140 km. We adopt a hierarchical strategy to conduct the joint inversion. First, we only carry out joint inversion using body wave arrival times and surface wave dispersion data. Then, we gradually increase data weighting for receiver functions to further constraint the Vs structure. To balance the contributions from different data types, we use the L-curve analysis method (Aster et al., 2013) to determine optimal data weights and regularization parameters (Fig. S5). From these L-curves, the optimal surface data weight α is chosen as 30 (Fig. S5a), the optimal data weight β for receiver function is 50 (Fig. S5b), the optimal damping parameter is 600 (Fig. S5c), and the optimal smoothing parameters for Vp and Vs models are $\eta_1 = 200$ and $\eta_2 = 300$, respectively.

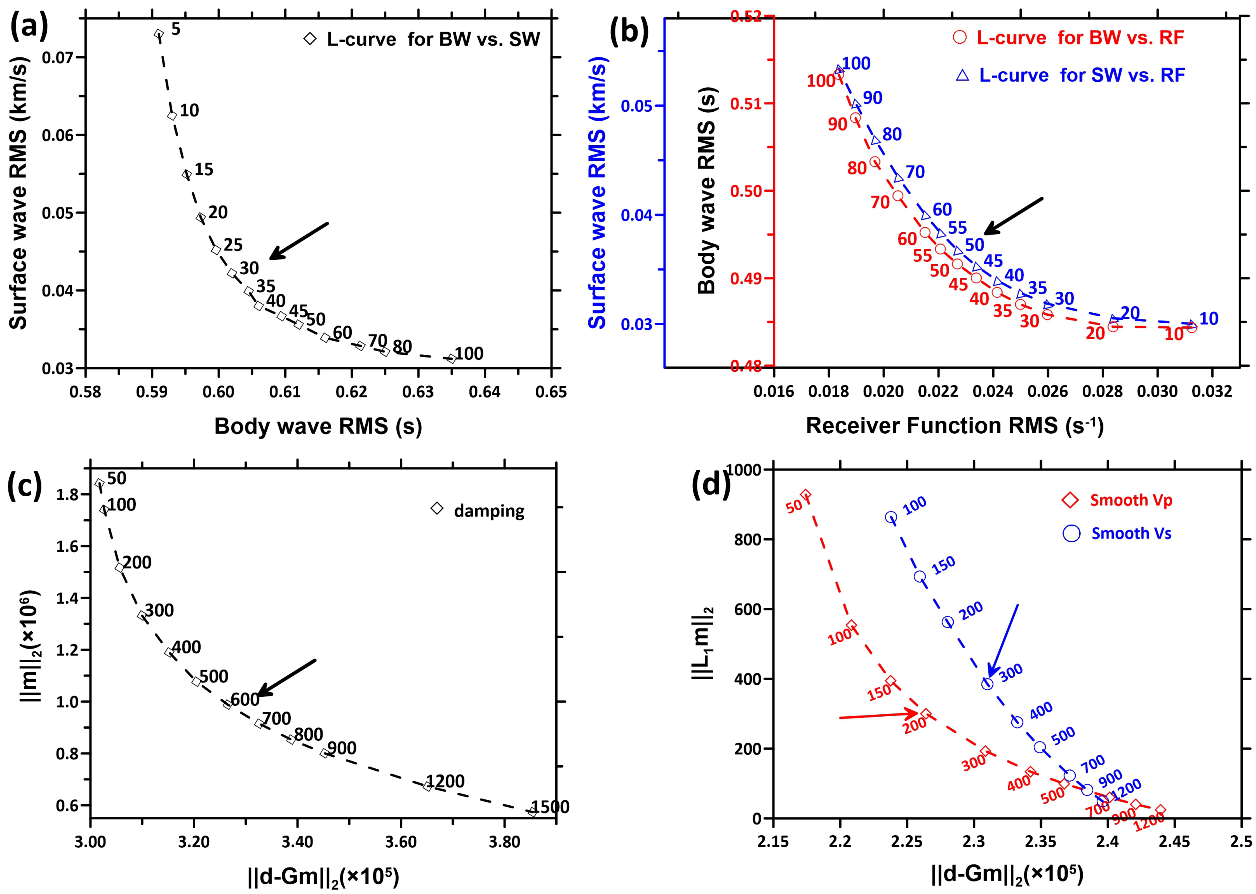

Figure S5. Selection of optimal parameters for joint inversion by the L-curve analysis. (a) The L-curve beween surface wave and body wave data residuals for different surface wave data weights, with the optimal weight α selected as 30. (b) The L-curve between receiver function data residual and surface wave data residual for different receiver function surface wave data weights (blue), and the L-curve between receiver function data residual and body wave data residual for different receiver function data weights (red). The optimal receiver function data weight β is selected as 50. (c) The L-curve between data residual and model norm for different damping parameters with the optimal damping parameter in LSQR selected as 600). (d) The L-curves between data residual and model smoothness for (red) Vp and (blue) Vs. The optimal smoothing parameters for Vp and Vs are $\eta_1 = 200$) and $\eta_2 = 300$.

12 iterations of the joint inversion are performed and the final velocity models are constrained to fit for three data types at the same time. The final root mean square (RMS) residuals of body

wave arrival times, surface wave dispersion data and receiver functions are 0.45s, 0.041 km/s and 0.019 s^{-1}, respectively. The distribution of residuals for these three data types is shown in Fig. S6. For P and S arrival times, the residuals after inversion are more concentrated around 0 s (Fig. S6a, b), and P and S RMS arrival time residuals are 0.38 s and 0.50 s, respectively. For surface wave dispersion data, the residuals are smaller than the uncertainties given by Shen et al. (2016). In comparison, the surface wave dispersion residuals in the Bohai Bay Basin are relatively large (Fig. S6c). For receiver functions, the fitting is relatively poor in the Bohai Bay Basin and central Ordos Basin (Fig. S6d), which is expected due to the contamination of multiples in the basins.

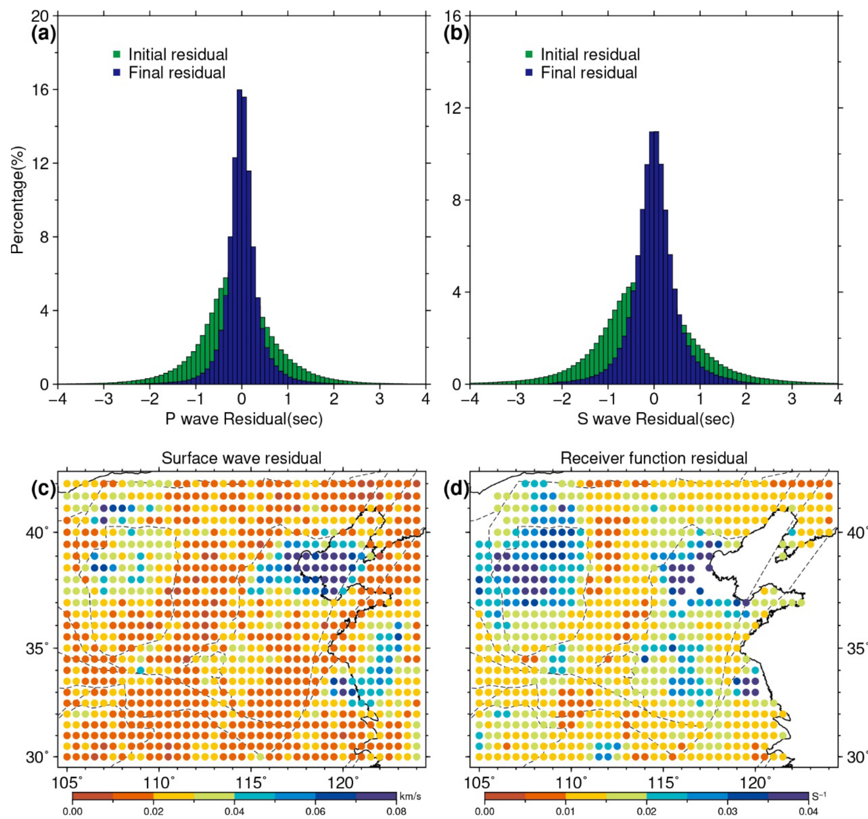

Figure S6. Distribution of residuals for different data types. (a) and (b) are the histograms of P- and S-wave travel time residuals (green) before and (blue) after joint inversion. (c) and (d) are the distribution of residuals for surface wave and receiver function data, respectively.

For further comparison, we selected 8 positions in the study area and compared the fitting of surface wave dispersion curve and receiver function (Fig. S7). It can be seen that the joint inversion results using three data types have a good fit for both surface wave dispersion data and receiver functions. In comparison, if only body wave arrival times and surface wave dispersion data are used for joint inversion, the resulting velocity models cannot fit receiver functions well.

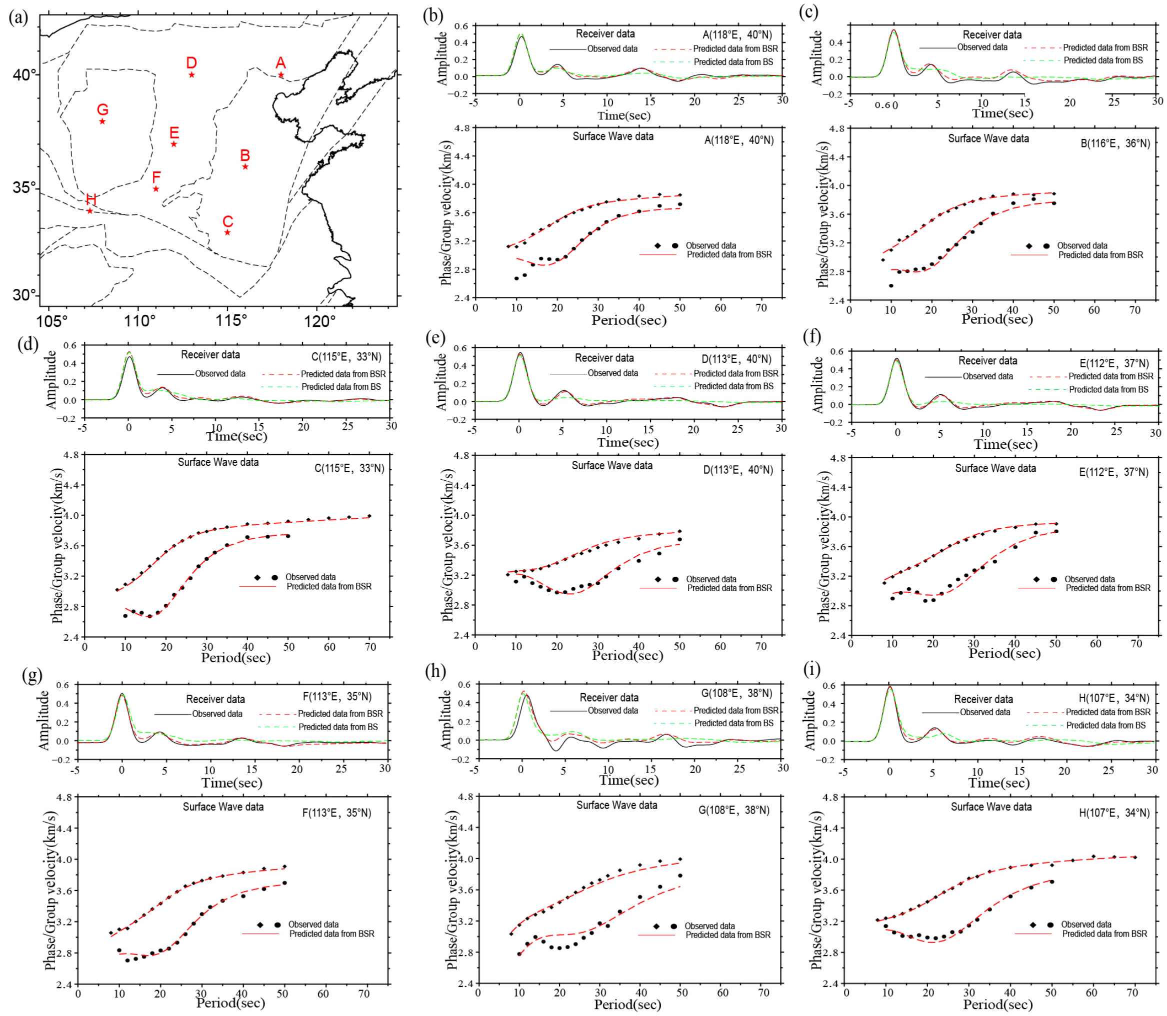

Figure S7. Comparison of surface wave dispersion curves and teleseismic receiver functions at 8 positions in the study area. The distribution of eight positions (red stars) is shown in (a). (b) to (i) show the fitting results of predicted and observed surface wave dispersion and receiver function data. For receiver functions, the black line denotes observed data, and the red and green lines denote predicted data based on velocity models from BSR joint inversion and BS joint inversion. For surface wave dispersion curves, diamonds and circles represent observed surface wave phase and group velocities, and red dashed lines represent predicted dispersion curves based on BSR joint inversion. BSR: body wave, surface wave and receiver function; BS: body wave and surface wave.

Because this joint inversion system can constrain Vs better than Vp, here we only focus on the Vs structure. Figs. 2 and 3 show depth slices and cross sections of the Vs model. For comparison, we also plotted the USTClitho2.0 Vs model (Han et al., 2022b), which is obtained by joint inversion of body wave arrival times and surface wave dispersion data (Fig. S8). It can be seen that because the depth resolution of the USTClitho2.0 Vs model is greater than 10 km (Han et al., 2022b), localized high velocity anomalies corresponding to the lithosphere delamination cannot be imaged. Only by the incorporation of receiver functions in the joint inversion in this study, we are able to image the delaminated lithosphere bodies in the Vs model. To better illuminate high velocity body anomalies, we also plot Vs perturbations with respect to average velocities at each depth along different latitudes and longitudes (Fig. S9). It can be seen high velocity bodies marked in Fig. 3 can be better delineated in velocity perturbations (Fig. S9). These high velocity bodies can also be better seen in the zoomed-in depth slices for the area of latitudes from 32° to 40° and longitudes from 110° to 120° (Fig. S10). It shows at depths of 95, 110, 125 and 140 km, high velocity bodies are evident from 112° to 118° in longitude.

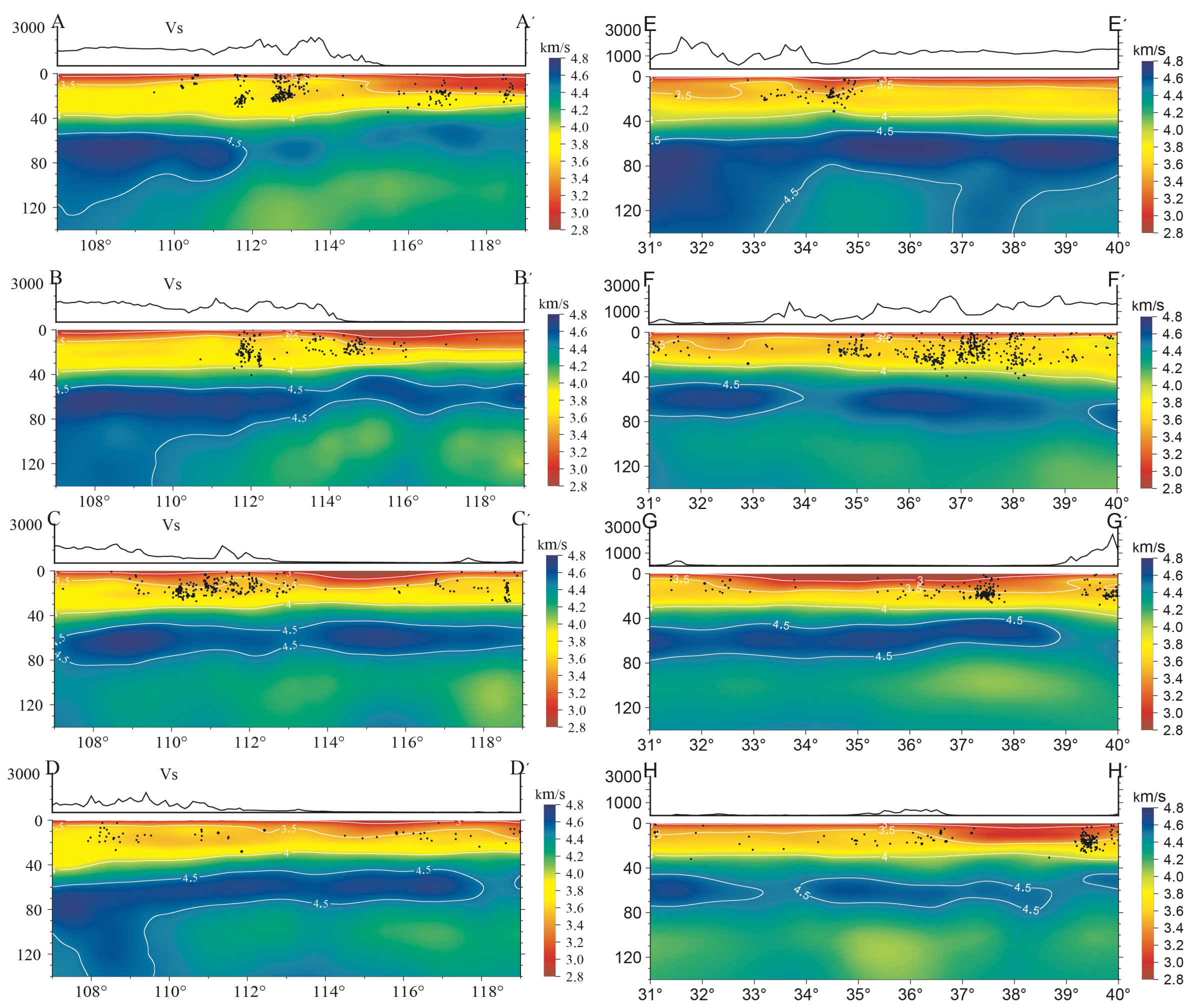

Figure S8. The same as Fig. 3 but for the USTClitho2.0 Vs model.

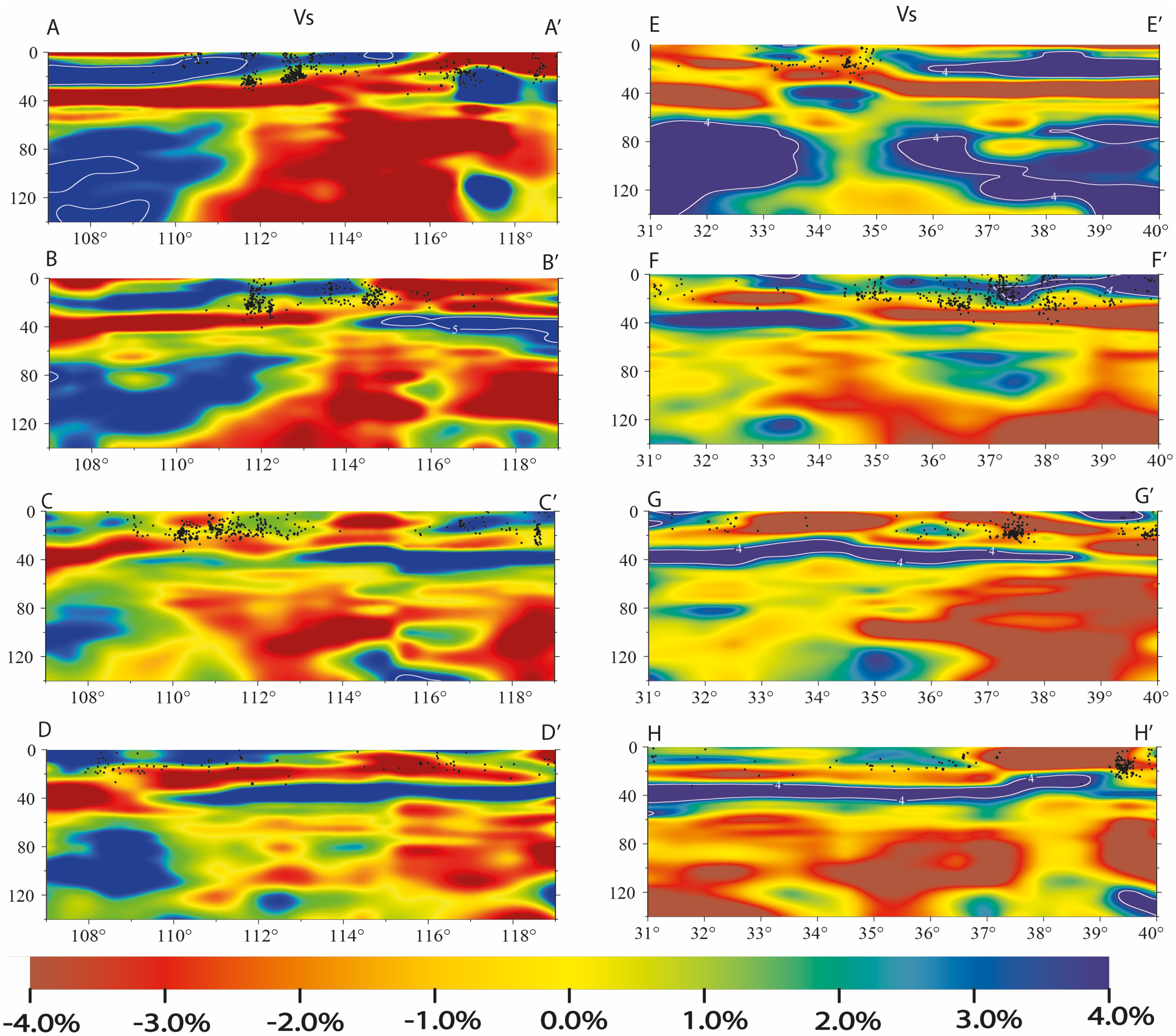

Figure S9. The same as Fig. 3 but for the Vs perturbations with respect to average velocities at each depth.

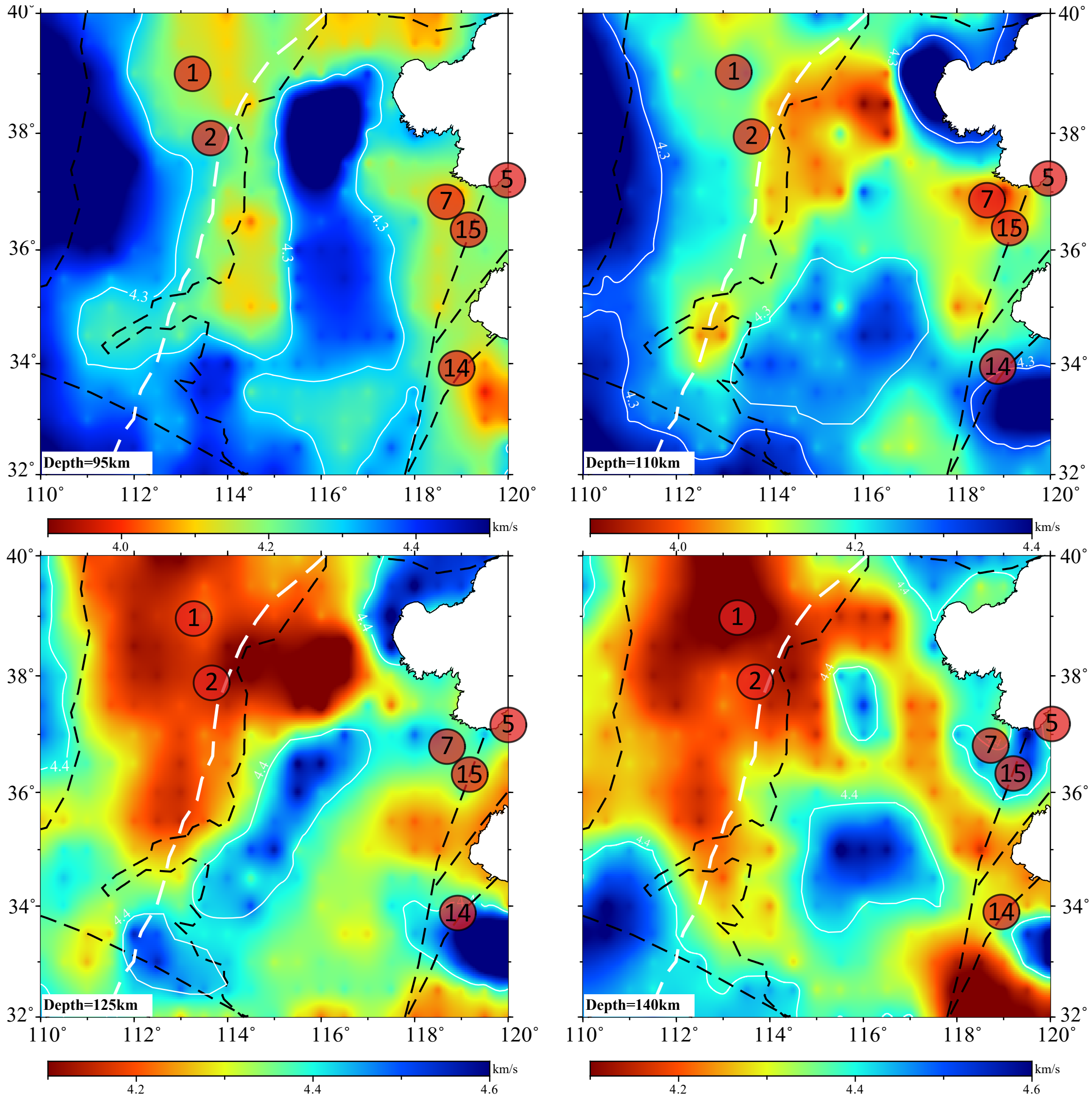

Figure S10. Horizontal slices of the Vs model at depths of 95. 110, 125, and 140 km from latitudes of 32° to 40°, and longitudes 110° to 120°. Cenozoic rock samples with εNd<0 are shown with the same markers in Figure 1.

We first use the checkerboard test（Humphreys and Clayton,1988）to evaluate the velocity model resolution. First, we add ±5% velocity perturbations to the initial models at adjacent grid nodes alternatively in three directions. Then we use the perturbed Vp and Vs models to calculate theoretical P and S arrival times, surface wave dispersion data, and receiver functions having the same data distribution as the real data. Then, Gaussian distributed noise with standard deviations of 0.1s and 0.2s is introduced for P and S arrival times, and Gaussian distributed noise with standard deviations of 0.03 km/s and 0.01s^{-1} is added to the surface wave dispersion and receiver function data, respectively. Finally, we perform joint inversion using these synthetic data to recover checkerboard models. Figs. S11 and S12 show recovered checkerboard models for Vs at different depths and along different sections. As seen for the depth slices of 95, 110 and 140 km, the checkerboard patterns are relatively well recovered between longitudes of 110° and 120°, where delaminated lithospheric bodies are seismically imaged. In comparison, at depth of 125 km, the checkerboard patterns are resolved relatively worse (Figs. S11, S12). However, by carefully checking the resolved checkerboard patterns for those imaged high velocity bodies below ~80-90 km, overall, the recovery is satisfactory. For example, for the imaged high velocity body in the depth range of 100-140 km and longitude range of 116°-118° along the AA' section (Fig. 3), the checkerboard patterns are resolved very well (Fig. S12). Along section BB', there are two high velocity bodies imaged in the longitude range of 116°-119° below depth of ~100 km (Fig. 3), which are also well resolved (Fig. S12). In addition, for the high velocity body imaged in the longitude range of 114°-117° below depth of 120 km (Fig. 3), the checkerboard recovery is also satisfactory (Fig. S12). In comparison, for the high velocity body imaged in the longitude range of 111.5°-114° below ~100 km (Fig. 3), the checkerboard recovery is relatively poor, indicating it may not be well resolved (Fig. S12).

It is known that checkerboard resolution test has its own limitations (Lévěque et al., 1993). To further check the reliability of high velocity bodies imaged in the asthenosphere shown in Fig. 3, we also conducted the model restoration test (Zhao et al.,1992). Except for using the final joint inversion Vp and Vs models as the synthetic velocity models, the process for the model restoration test is the same as the checkerboard test. The comparison of input and recovered Vs models along 8 profiles in Fig. 1b are shown in Figs. S13-S16, respectively. It can be seen that those marked high velocity bodies that are interpreted as delaminated lithosphere can be well recovered. By combining model checkerboard and restoration test results, it can be inferred that the lithospheric Vs structure of north China craton obtained in this study is reliable.

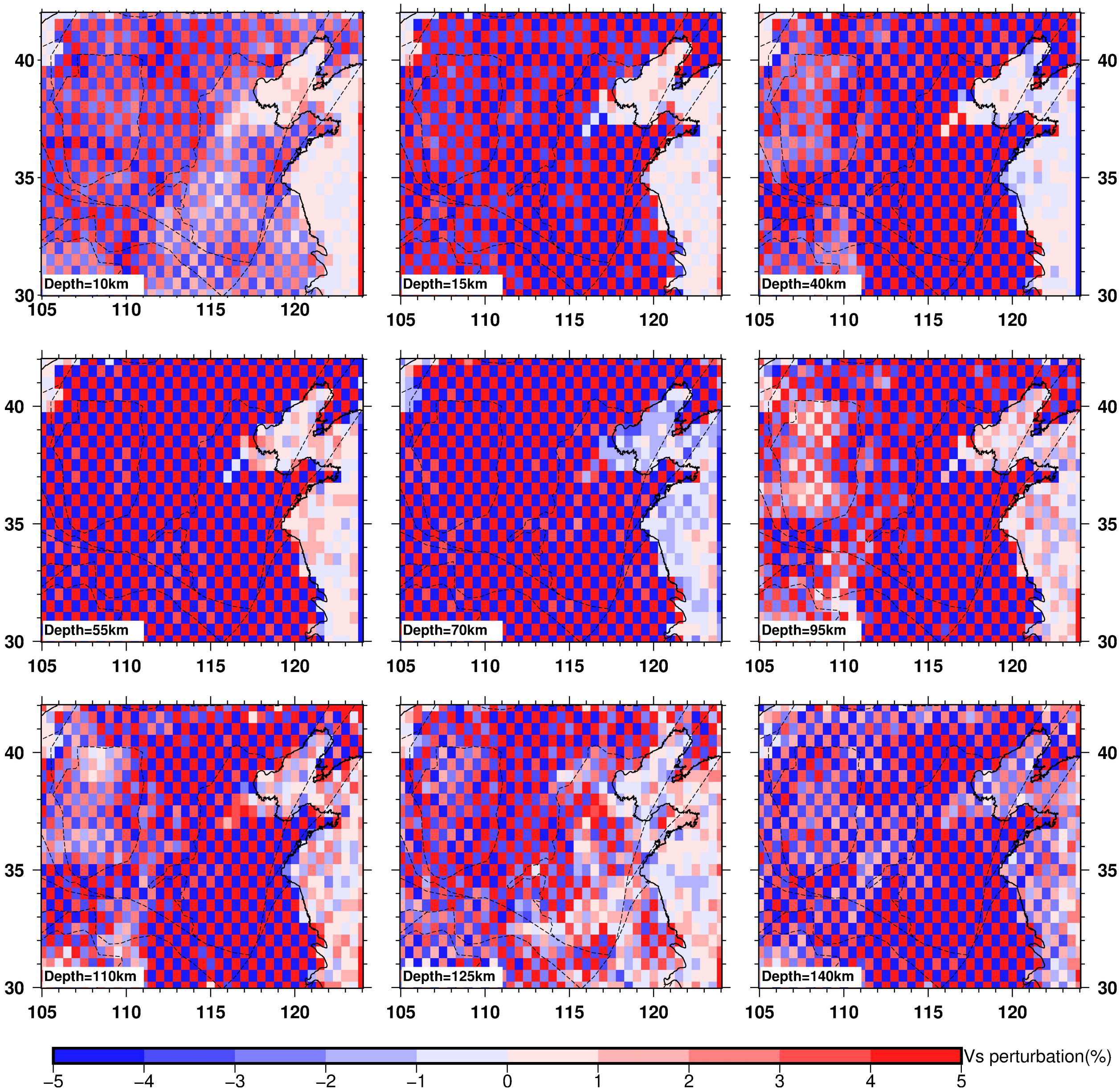

Figure S11. Recovered checkerboard patterns for Vs at different depths by joint inversion of body wave, surface wave, and receiver function data.

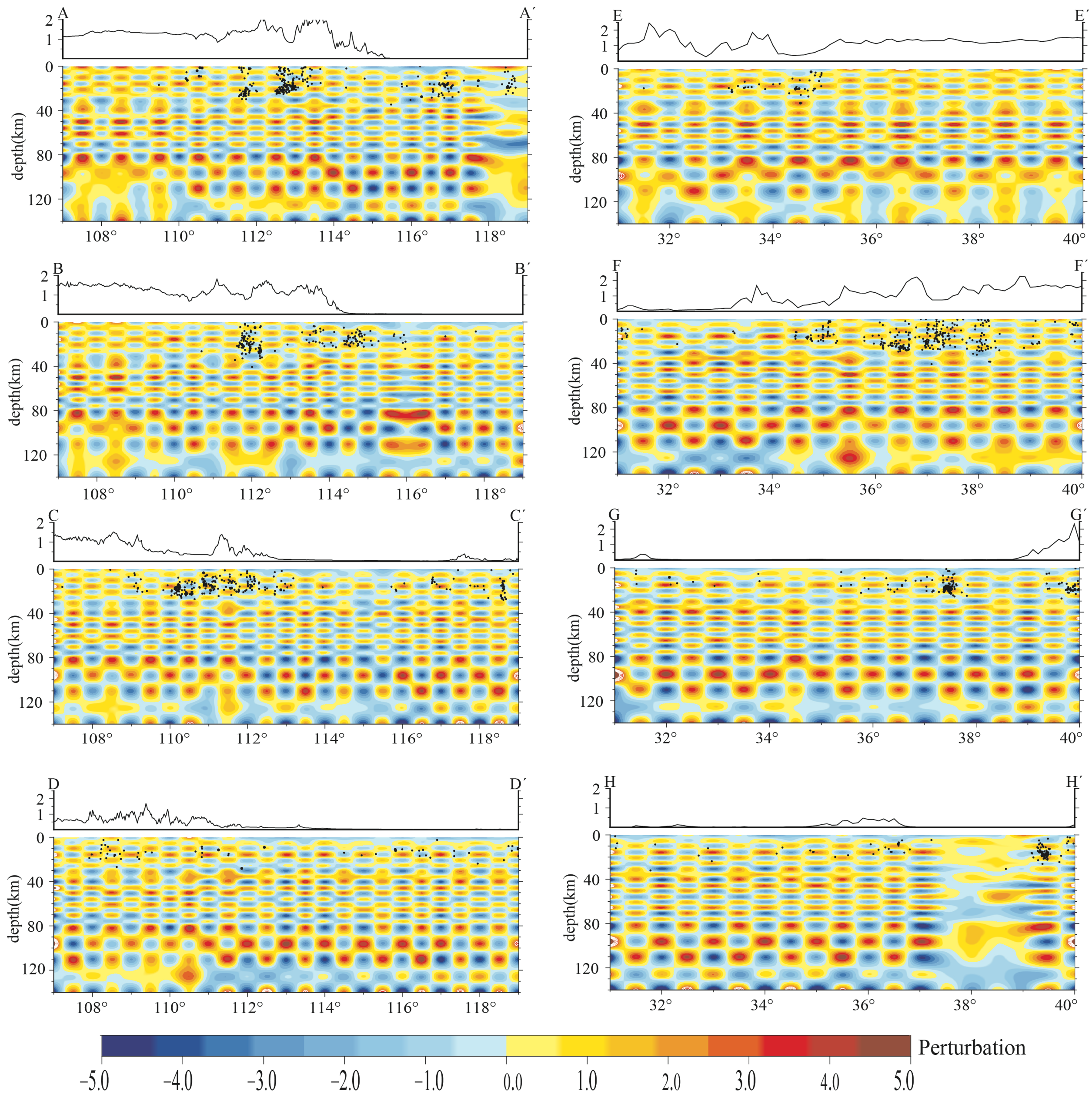

Figure S12. Recovered checkerboard patterns for Vs along eight profiles in Figure 1 by joint inversion of body wave, surface wave, and receiver function data.

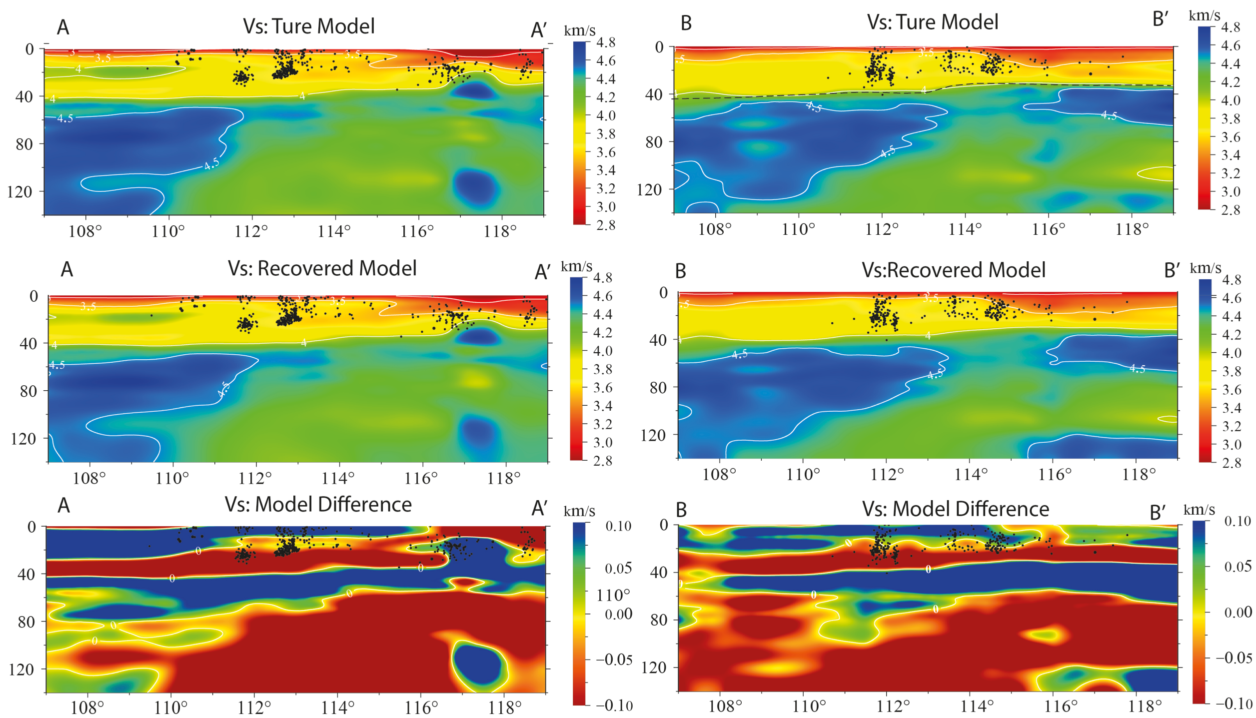

Figure S13. The restoration test results along profiles AA' and BB'. The first row is the input Vs model from real data joint inversion, the second row is the recovered Vs model, and the third row is the Vs differences of the two models. The profile locations are marked in Fig. 1b.

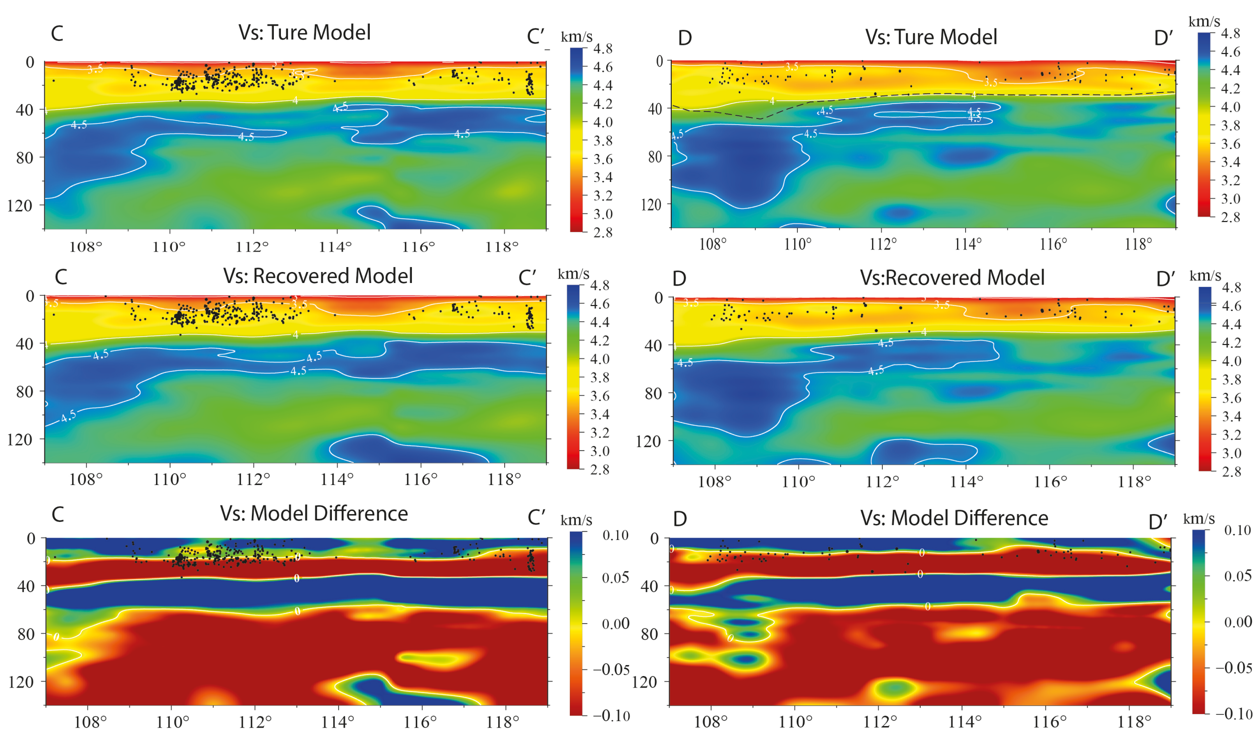

Figure S14. Same as Fig. S13 but for profiles CC' and DD'

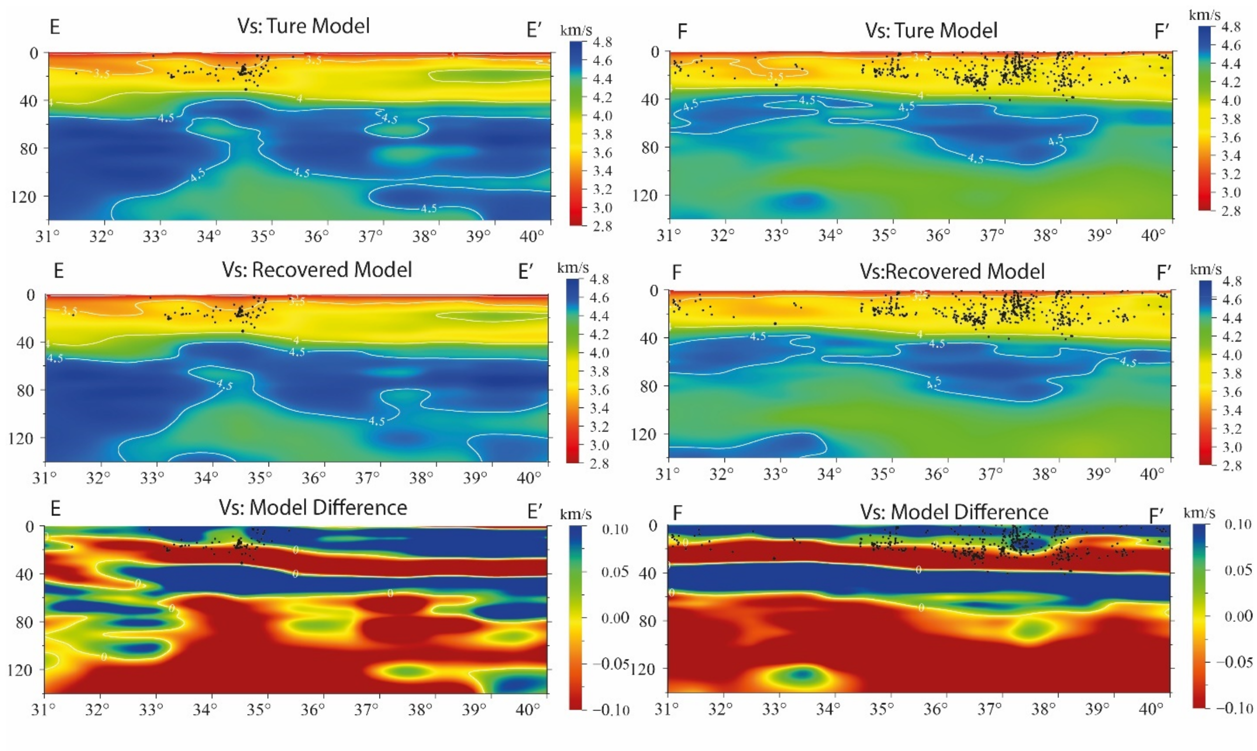

Figure S15. Same as Fig. S13 but for profiles EE' and FF'

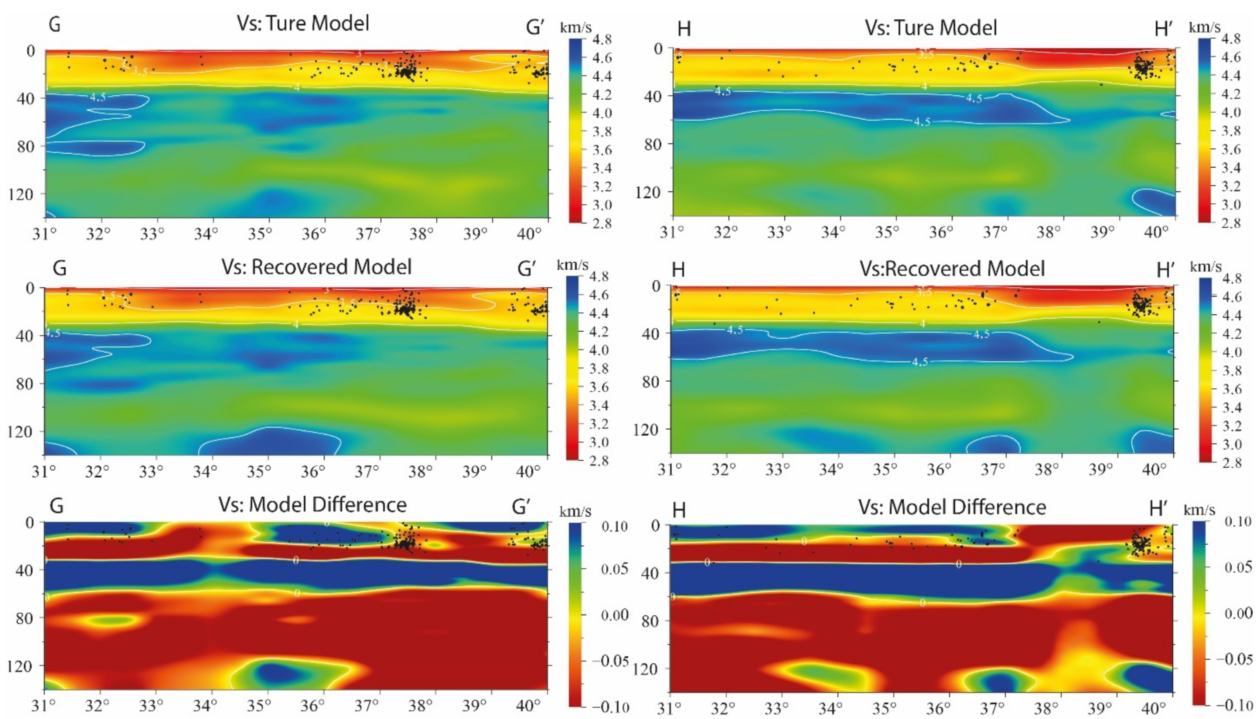

Figure S16. Same as Fig. S13 but for profiles GG' and HH'

Table S1 Nd isotope data for Cenozoic basalts in the North China Craton

Sample	Location in Fig. 1	Age (Ma)	$^{143}Nd/^{144}Nd$	$\varepsilon_{Nd}(t)$	Ref.
11NW01	3	0	0.512521	-2.3	Fan et al., 2014
11NW02	3	0	0.512678	0.8	
13NW06	3	0			
13NW07	3	0			
11NW04	3	0	0.512781	2.8	
11NW03	3	0	0.512587	-1.0	
11NW05	3	0	0.512562	-1.5	
11NW11	3	0			
11NW06	3	0	0.512778	2.7	
13NW10	3	0			
11NW07	3	0	0.512769	2.6	
11NW08	3	0	0.512716	1.5	
11NW09	3	0	0.51271	1.4	
YYG-03	4	23.4	0.512893	5.2	Guo et al., 2014
YYG-17	4	23.4	0.512849	4.3	
DB-01	4	21.9	0.512967	6.6	
DB-02	4	21.9	0.512957	6.4	
DB-03	4	21.9	0.512972	6.7	
DB-07	4	21.9	0.512889	5.1	
BYCGI-03	4	1	0.512724	1.7	
BYCGII-02	4	1	0.512791	3.0	
BYCGm-05	4	1	0.512857	4.3	
BYCGm-12	4	1	0.512838	3.9	
SBL-06	5	5.03	0.512898	5.1	Lee et al., 2006
SBL-09	5	5.11	0.512885	4.9	
SBL-10	5	5.17	0.512924	5.6	
SBL-G7	5	5.62	0.512807	3.3	
SQX-05	5	6.45	0.512859	4.4	
SQX-10	5	6.18	0.512835		
SP13	5	5	0.512781	2.8	
SLJ-54	7	13.43	0.512933	5.9	
SS4	7	1	0.512826	3.7	
SLJ-72	7	13.72	0.512621	-0.2	
SLJ-74	7	12.63	0.512949	6.2	
SLJ-77	7	13	0.512825	3.7	
SYS-04	15	12.84	0.512907		
SYS-05	15	13.6	0.512908		
SYS-15	15	14.02	0.512966		
Y181	6	46.9	0.512743	2.4	Li et al., 2014
Y182	6	46.9	0.512756	2.7	

Y183	6	46.9	0.512758	2.8	
Y184	6	46.9	0.51276	2.8	
Y185	6	46.9	0.512758	2.8	
Y186	6	46.9	0.512763	2.9	
Y2507	6	45.5	0.512876	5.1	
Y2508	6	45.5	0.512879	5.2	
Y2509	6	45.5	0.512872	5.0	
Y2510	6	45.5	0.512881	5.2	
SD1301	6	1	0.512913	5.4	Sakuyama et al., 2013
SD1302	6	1	0.512910	5.3	
SD1303	6	1	0.512899	5.1	
SD1304	6	1	0.512929	5.7	
SD1405	7	20	0.512885	5.0	
SD1406	7	20	0.512921	5.7	
SD1407	7	20	0.512879	4.9	
SD1508	7	20	0.512872	4.8	
SD1508-2	7	20	0.512818	3.7	
05HF02	8	38	0.512804	3.5	Wang et al., 2011
05HF04	8	38	0.512803	3.5	
05HF08	8	38	0.512799	3.4	
05HF09	8	38	0.512797	3.4	
06SW37	10	16	0.512831	3.9	
06SW45	10	16	0.512746	2.2	
06SW47	10	16	0.512738	2.1	
06SW48	10	16	0.512724	1.8	
06SW49	10	16	0.512742	2.1	
06SW50	10	16	0.512762	2.5	
05HF10	9	38	0.512937	6.2	
05HF15	9	38	0.512919	5.8	
05HF17	9	38	0.512816	3.8	
05HF18	9	38	0.512876	5.0	
06SW03	13	6	0.51297	6.5	
06SW04	13	6	0.512963	6.4	
06SW05	13	6	0.512964	6.4	
06SW07	13	6	0.51297	6.5	
06SW08	13	6	0.512949	6.1	
06SW09	12	7	0.51299	6.9	
06SW11	12	7	0.512985	6.8	
06SW12	12	7	0.512955	6.2	
06SW13	12	7	0.512985	6.8	
06SW15	12	7	0.512975	6.6	
05NS02	11	0.6	0.513011	7.3	
05NS04	11	0.6	0.513002	7.1	
08PSS01	14	16	0.513019	7.6	Zeng et al., 2013
08PSS02	14	16	0.513003	7.3	

08PSS03	14	16	0.513019	7.6	
08PSS04	14	16	0.513007	7.4	
08PSS05	14	16	0.513008	7.4	
08PSS06	14	16	0.513005	7.3	
08PSS07	14	16	0.513006	7.3	
08PSS08	14	16	0.513016	7.5	
08TS03	14	16	0.512995	7.1	
08TS05	14	16	0.512984	6.9	
05WD06	14	16	0.512667	0.7	Zhang et al., 2009
05WD08	14	16	0.512679	0.9	
05WD09	14	16	0.512554	-1.5	
05WD15	14	16	0.512671	0.8	
05WD16	14	16	0.512723	1.8	
05WD31	14	16	0.512887	5.0	
05WD33	14	16	0.512900	5.2	
06WD38	14	16	0.512842	4.1	
05WD42	14	16	0.512531	-2.0	
06SW19	14	16	0.512940	6.0	
06SW21	14	16	0.512983	6.9	
06SW23	14	16	0.512966	6.5	
06SW30	14	16	0.512751	2.3	
06SW31	14	16	0.512749	2.3	
06SW34	14	16	0.512899	5.2	
06SW35	14	16	0.512897	5.2	
05WD11	14	16	0.512657	0.5	
05WD18	14	16	0.512823	3.7	
05WD22	14	16	0.512648	0.3	
06SW25	14	16	0.512915	5.5	
05WD05	14	16	0.512239	-7.7	
05WD36	14	16	0.512475	-3.1	
05WD39	14	16	0.512421	-4.1	
05WD41	14	16	0.512525	-2.1	
06SW26	14	16	0.512744	2.2	
06SW28	14	16	0.512558	-1.5	
06SW33	14	16	0.512615	-0.4	
CH-7	3	10	0.512586	-1.0	Zhang et al., 2012
CH-6	3	10	0.512588	-0.9	
CH-5	3	10	0.512580	-1.1	
CH-4	3	10	0.512635	0.0	
CH-3	3	10	0.512565	-1.4	
CH-2	3	10	0.512651	0.3	
CH-1	3	10	0.512661	0.5	
XA-1	3	10	0.512728	1.8	
XA-2	3	10	0.512848	4.1	
XA-3	3	10	0.512693	1.1	

XA-5	3	10	0.512678	0.8	
XA-6	3	10	0.512733	1.9	
HQ-2	3	22	0.512695	1.2	
HQ-3	3	22	0.512705	1.4	
HQ-6	3	22	0.512647	0.3	
HQ-8	3	22	0.512686	1.0	
HQ-10	3	22	0.512567	-1.3	
BY-2	3	33	0.512554	-1.4	
BY-3	3	33	0.512651	0.4	
BY-5	3	33	0.512583	-0.9	
BY-6	3	33	0.512455	-3.4	
DL-5	3	33	0.512583	-0.9	
07NIS01	7	20	0.512812	3.6	Zeng et al., 2011
07NIS02	7	20	0.512821	3.8	
07NIS03	7	20	0.512826	3.8	
07NIS04	7	20	0.512824	3.8	
07SW01	7	20	0.512641	0.2	
07SW02	7	20	0.512635	0.1	
07SW03	7	20	0.512565	-1.3	
07FYS01	7	20	0.512628	0.0	
07FYS02	7	20	0.512633	0.1	
07FYS03	7	20	0.51263	0.0	
07FYS04	7	20	0.512735	2.1	
07FYS05	7	20			
07FYS06	7	20	0.512824	3.8	
07FYS07	7	20	0.512936	6.0	
07FYS09	7	20	0.512726	1.9	
07FYS10	7	20	0.512741	2.2	
07THS01	7	20	0.512937	6.0	
07THS02	7	20	0.512927	5.8	
07THS03	7	20	0.512934	6.0	
07FS01	7	20	0.512906	5.4	
07FS02	7	20	0.512915	5.6	
07FS03	7	20	0.512887	5.1	
07LS04	15	13	0.512835	4.0	
07LS05	15	13	0.512836	4.0	
07LS06	15	13	0.512824	3.8	
07LS07	15	13	0.512847	4.2	
07CDS01	15	13	0.512623	-0.2	
07CDS02	15	13	0.512629	-0.1	
07CDS04	15	13	0.512617	-0.3	
07CDS05	15	13	0.512612	-0.4	
07CDS06	15	13	0.5126	-0.6	
07CDS07	15	13	0.512592	-0.8	
07LIS01	15	13	0.512902	5.3	

07LIS02	15	13	0.51277	2.7	
07LIS03	15	13	0.512714	1.6	
07LIS04	15	13	0.512774	2.8	
07LIS05	15	13	0.512715	1.6	
FS-1	1	24.4	0.512795	3.3	Tang et al., 2006
FS-8	1	24.4	0.512747	2.3	
FS-10	1	25.8	0.512755	2.5	
FS-30	1	25.8	0.512796	3.3	
FS-32	1	26.3	0.512731	2.1	
FS-33	1	26.3	0.51275	2.4	
HHL-1	1	25.7	0.512708	1.6	
HHL-2	1	25.7	0.512733	2.1	
FS-2	1	24.3	0.512427	-4.0	
FS-3	1	24.3	0.51254	-1.7	
FS-9	1	24.3	0.512541	-1.7	
FS-36	1	24.3	0.512634	0.1	
FS-38	1	25	0.5126	-0.5	
JX-1	2	7.3	0.512731	1.9	
JX-3	2	7.3	0.512895	5.1	
FHS-1	2	7.3	0.512689	1.1	
MAS-1	2	7.7	0.512819	3.6	
JD-1	2	7.9	0.512847	4.1	
GB-2	2	7.9	0.512821	3.6	
ZQ-1	16	5.6	0.512651	0.3	
ZQ-2	16	5.6	0.512658	0.4	
ZQ-4	16	5.6	0.512638	0.0	

References

Aster, R C, Borchers, B, Thurber, C H. 2013. Parameter Estimation and Inverse Problems (second edition)[M]: Academic press Waltham, MA

Chai, C, Ammon, C J, Maceira, M, Herrmann, R B. 2015. Inverting interpolated receiver functions with surface wave dispersion and gravity: Application to the western U.S. and adjacent Canada and Mexico[J]. Geophysical Research Letters, 42(11): 4359-4366

Fan, Q. C., Chen, S. S., Zhao, Y. W., Zou, H. B., Li, N., & Sui, J. L. (2014). Petrogenesis and evolution of Quaternary basaltic rocks from the Wulanhada area, North China. Lithos, 206, 289-302.

Fang, H, Zhang, H, Yao, H, Allam, A, Zigone, D, Ben - Zion, Y, Thurber, C, van der Hilst, R D. 2016. A new algorithm for three - dimensional joint inversion of body wave and surface wave data and its application to the Southern California plate boundary region[J]. Journal of Geophysical Research: Solid Earth, 121(5): 3557-3569

Guo, P., Niu, Y., Ye, L., Liu, J., Sun, P., Cui, H., ... & Feng, Y. (2014). Lithosphere thinning beneath west North China Craton: evidence from geochemical and Sr–Nd–Hf isotope compositions of Jining basalts. Lithos, 202, 37-54.

Han, S, Zhang, H, Gao, L, Chai, C, Maceira, M. 2022a. Joint inversion of body wave arrival times, surface wave dispersion data and receiver functions: Method and Application to south China[J]. Journal of Geophysical Research: Solid Earth, 44: 1-16

Han, S, Zhang, H, Xin, H, Shen, W, Yao, H. 2022b. USTClitho2.0: Updated Unified Seismic Tomography Models for Continental China Lithosphere from Joint Inversion of Body-Wave Arrival Times and Surface-Wave Dispersion Data[J]. Seismological Research Letters, 93(1): 201-215

Humphreys, E, Clayton, R W. 1988. Adaptation of back projection tomography to seismic travel time problems[J]. Journal of Geophysical Research, 93(B2)

Julia, J, Ammon, C J, Herrmann, R B, Correig, A M. 2000. Joint inversion of receiver function and surface wave dispersion observations[J]. Geophysical Journal International, 143(1): 99-112

Lee, Y. T., Chen, J. C., Shih, J. Y., Juang, W. S., Yang, H. J., Huang, S. W., & Lin, M. L. (2006). Geochemistry of Cenozoic basaltic rocks from Shandong Province and its implication for mantle process in North China. Geochemical Journal, 40(6), 579-596.

Lévěque, J. J., Rivera, L., & Wittlinger, G. 1993. On the use of the checkerboard test to assess the resolution of tomographic inversions. Geophysical Journal International, 115(1), 313-318.

Li, H. Y., Huang, X. L., & Guo, H. (2014). Geochemistry of Cenozoic basalts from the Bohai Bay Basin: Implications for a heterogeneous mantle source and lithospheric evolution beneath the eastern North China Craton. Lithos, 196, 54-66.

Ligorrfa, J P, Ammon, C J. 1999. Iterative deconvolution and receiver-function estimation[J]. Bull.Seismolo.Soc.Am, 89(5): 1395-1400

Paige, C C, Saunders, M A. 1982. LSQR: an algorithm for sparse linear equations and sparse least squares[J]. Trans. Math. Softw, 8(1): 43-71

Sakuyama, T., Tian, W., Kimura, J. I., Fukao, Y., Hirahara, Y., Takahashi, T., ... & Tatsumi, Y. (2013). Melting of dehydrated oceanic crust from the stagnant slab and of the hydrated mantle

transition zone: Constraints from Cenozoic alkaline basalts in eastern China. Chemical Geology, 359, 32-48.
Shen, W, Ritzwoller, M H, Kang, D, Kim, Y, Lin, F-C, Ning, J, Wang, W, Zheng, Y, Zhou, L. 2016. A seismic reference model for the crust and uppermost mantle beneath China from surface wave dispersion[J]. Geophysical Journal International, 206(2): 954-979
Tang, Y. J., Zhang, H. F., & Ying, J. F. (2006). Asthenosphere–lithospheric mantle interaction in an extensional regime: implication from the geochemistry of Cenozoic basalts from Taihang Mountains, North China Craton. Chemical Geology, 233(3-4), 309-327.
Wang, Y., Zhao, Z. F., Zheng, Y. F., & Zhang, J. J. (2011). Geochemical constraints on the nature of mantle source for Cenozoic continental basalts in east-central China. Lithos, 125(3-4), 940-955.
Zeng, G., Chen, L. H., Hofmann, A. W., Jiang, S. Y., & Xu, X. S. (2011). Crust recycling in the sources of two parallel volcanic chains in Shandong, North China. Earth and Planetary Science Letters, 302(3-4), 359-368.
Zeng, G., Chen, L. H., Hu, S. L., Xu, X. S., & Yang, L. F. (2013). Genesis of Cenozoic low - Ca alkaline basalts in the Nanjing basaltic field, eastern China: The case for mantle xenolith - magma interaction. Geochemistry, Geophysics, Geosystems, 14(5), 1660-1677.
Zhang, H, Lu, Q T, Wang, X L, Han, S, Liu, L, Gao, L, Wang, R, Hou, Z Q. 2023. Seismically imaged lithospheric delamination and its controls on the Mesozoic Magmatic Province in South China[J]. Nat Commun, 14(1): 2718
Zhang, H, Maceira, M, Roux, P, Thurber, C. 2014. Joint Inversion of Body-Wave Arrival Times and Surface-Wave Dispersion for Three-Dimensional Seismic Structure Around SAFOD[J]. Pure and Applied Geophysics, 171(11): 3013-3022
Zhang, H, Thurber, C. 2003. Double-Difference Tomography: The Method and Its Application to the Hayward Fault, California[J]. Bulletin of the Seismological Society of America, 93(5): 1875–1889
Zhang, H, Thurber, C. 2006. Development and Applications of Double-difference Seismic Tomography[J]. Pure and Applied Geophysics, 163(2-3): 373-403
Zhang, J. J., Zheng, Y. F., & Zhao, Z. F. (2009). Geochemical evidence for interaction between oceanic crust and lithospheric mantle in the origin of Cenozoic continental basalts in east-central China. Lithos, 110(1-4), 305-326.
Zhang, W. H., Zhang, H. F., Fan, W. M., Han, B. F., & Zhou, M. F. (2012). The genesis of Cenozoic basalts from the Jining area, northern China: Sr–Nd–Pb–Hf isotope evidence. Journal of Asian Earth Sciences, 61, 128-142.
Zhao, D., Hasegawa, A. and Horiuchi, S., 1992. Tomographic imaging of P and S wave velocity structure beneath northeastern Japan. Journal of Geophysical Research: Solid Earth, 97(B13), pp.19909-19928.